

Experimental quantum channel simulation

He Lu,^{1,2} Chang Liu,^{1,2} Dong-Sheng Wang,³ Luo-Kan Chen,^{1,2} Zheng-Da Li,^{1,2} Xing-Can Yao,⁴ Li Li,^{1,2} Nai-Le Liu,^{1,2} Cheng-Zhi Peng,^{1,2} Barry C. Sanders,^{1,2,3,5} Yu-Ao Chen,^{1,2} and Jian-Wei Pan^{1,2}

¹*Shanghai Branch, National Laboratory for Physical Sciences at Microscale and Department of Modern Physics, University of Science and Technology of China, Shanghai 201315, China*

²*Synergetic Innovation Center of Quantum Information and Quantum Physics, University of Science and Technology of China, Hefei, Anhui 230026, China*

³*Institute for Quantum Science and Technology, University of Calgary, Alberta T2N 1N4, Canada*

⁴*Physikalisches Institut, Ruprecht-Karls-Universität Heidelberg, Im Neuenheimer Feld 226, 69120 Heidelberg, Germany*

⁵*Program in Quantum Information Science, Canadian Institute for Advanced Research, Toronto, Ontario M5G 1Z8, Canada*

Quantum simulation is of great importance in quantum information science. Here, we report an experimental quantum channel simulator imbued with an algorithm for imitating the behavior of a general class of quantum systems. The reported quantum channel simulator consists of four single-qubit gates and one controlled-NOT gate. All types of quantum channels can be decomposed by the algorithm and implemented on this device. We deploy our system to simulate various quantum channels, such as quantum-noise channels and weak quantum measurement. Our results advance experimental quantum channel simulation, which is integral to the goal of quantum information processing.

I. INTRODUCTION

Quantum simulation [1–3] is the most promising near-term application of quantum computing due to the resource requirements for imitating some classically intractable systems being significantly less onerous than for other applications such as factorization. Experimental quantum simulation on closed systems is well studied using photons [4], atoms [5] and trapped ions [6]. Quantum simulation of open-system dynamics also has variety of applications, such as dissipative quantum phase transitions [7] and dissipative quantum-state engineering [8], thermalization [9], quantum noise generators [10], non-Markovian dynamics [11], and non-unitary quantum computing [12]. Although any non-unitary quantum dynamics could be embedded into unitary dynamics over a larger Hilbert space with Hamiltonian evolution [13], such a direct approach entails a large computational-space overhead and resultant experimental complexity. Previous experiments have demonstrated a universal unitary-gate on a reprogrammable waveguide chip [14] and have explored some open-system single-qubit dynamics such as quantum noise [15–17], weak measurement [18, 19] and transpose [20–22].

Our approach is quite distinct from these prior achievements in that our one apparatus simulates all these transformations and more, in fact *any* single-qubit channel. We aim to realize a digital single-qubit channel simulator, which will serve as reconfigurable component of a nonunitary quantum circuit that would simulate nonunitary circuits. Furthermore our quantum simulator is “digital”. A digital quantum simulator is more versatile, as it is able to simulate a wider range of Hamiltonians[5]. In the sense of the analog-digital quantum simulation dichotomy [3], for which a digital quantum simulator can be expressed as a concatenation of a primitive quantum instruction set comprising, for example, single-qubit gates and a controlled-not (CNOT) gate. In fact our qubit-channel quantum simulator requires just one CNOT gate and

one ancillary qubit, hence is minimal in two-qubit gate cost, whereas ten two-qubit gates and two ancillary qubits are required using standard Stinespring dilation [23]. Our quantum simulator also uses far fewer single-qubit rotations than Stinespring dilation would yield [24].

In this article, we report an experimental quantum simulator which is imitated by a decomposition algorithm. Any single qubit channel can be decomposed into a mixture of two quasi-extreme channels. Experimentally, the quasi-extreme channel is implemented by using optical technology and the mixture of two quasi-extreme channels is realized by combining the collected data from two quasi-extreme channels.

The article is organized as follows. Sec. II provides a theoretical introduction to channel decomposition and numerical simulation of the decomposition algorithm. Sec. III describes the experimental setup. In Sec. IV we present the experimental results, including four individual quantum noise channels and a simulation of weak measurement process. Finally, Sec. V contains discussion and conclusions.

II. THEORY

We construct a quantum channel simulator that transforms a photonic qubit approximately according to any channel \mathcal{E} [24], which is a linear, trace-nonincreasing completely positive map that maps quantum state ρ to $\mathcal{E}(\rho)$. The approximate experimental channel \mathcal{E}_{exp} is guaranteed to map within a pre-specified error tolerance ϵ with respect to \diamond -distance d_\diamond , which is the metric for quantifying the worst-case distinguishability of the approximate from the true final state according to trace distance. Our classical algorithm for designing a qubit-channel simulating circuit accepts ϵ and a 4×4 matrix description of \mathcal{E} as input and yields a description $[\mathcal{C}]$ of the photonic circuit \mathcal{C} as output with \mathcal{C} comprising single-qubit and a single two-qubit gate plus classical bits. A single-

qubit channel can be expressed as

$$\mathcal{E}(\rho) = \sum_{i,j=0}^3 \mathcal{E}_{ij} \Xi_i \rho \Xi_j, \quad \Xi = (\mathbf{1}, \boldsymbol{\sigma}) \quad (1)$$

with $\mathbf{1}$ the 2×2 identity operator and $\boldsymbol{\sigma} = (X, Y, Z)$ the Pauli matrices.

For any single-qubit channel \mathcal{E} , $p \in [0, 1]$ exists such that

$$\mathcal{E} = p\mathcal{E}_1^c + (1-p)\mathcal{E}_2^c \quad (2)$$

for each \mathcal{E}_i^c a generalized extreme channel [24]. An arbitrary generalized extreme channel \mathcal{E}^c is specified by two Kraus operators

$$M_i = R_{\mathbf{n}}(2\varphi)K_iR_{\mathbf{m}}(2\delta), \quad R_{\mathbf{r}}(2\theta) := \exp(-i\theta\mathbf{r} \cdot \boldsymbol{\sigma}) \quad (3)$$

and

$$K_0 = \begin{pmatrix} \cos \beta & 0 \\ 0 & \cos \alpha \end{pmatrix}, \quad K_1 = \begin{pmatrix} 0 & \sin \alpha \\ \sin \beta & 0 \end{pmatrix}, \quad (4)$$

for $0 \leq \alpha, \beta \leq 2\pi$. Furthermore, the Kraus operators K_i can be realized by the circuit shown in Fig. 1a. In the circuit,

$$R_y(2\gamma) = \exp(-iY\gamma) = \mathbf{1} \cos \gamma - iY \sin \gamma, \quad (5)$$

and

$$2\gamma_{1,2} = \beta \mp \alpha \pm \frac{\pi}{2}. \quad (6)$$

Each \mathcal{E}_i^c has eight parameters leading to 17 parameters (including p) for arbitrary \mathcal{E} . Random \mathcal{E} is generated as a two-qubit partial trace of a three-qubit Haar-random $SU(8)$ matrix. Decomposing into Kraus operators (3) is achieved by guessing the 17 parameters and then optimizing by reducing the distance between the trial channel and the desired channel \mathcal{E} . When the trial channel \mathcal{E}' is sufficiently close to \mathcal{E} , the optimization routine terminates with the 17-parameter decomposition as output.

We test the decomposing algorithm by numerical simulation. In the numerical simulation, an arbitrary channel is generated from a randomly chosen unitary operator $U \in SU(8)$ and the channel form can be derived from Kraus operators $K_i = \langle i|U|0\rangle$. Five examples of input channels are

$$\mathcal{C}_1 = \begin{pmatrix} 0.9276 + 0.0000i & 0.1125 + 0.0039i & -0.0027 - 0.0150i & -0.1900 - 0.3383i \\ 0.1125 - 0.0039i & 0.4846 + 0.0000i & 0.0210 + 0.0554i & 0.0787 - 0.1229i \\ -0.0027 + 0.0150i & 0.0210 - 0.0554i & 0.0724 + 0.0000i & -0.1125 - 0.0039i \\ -0.1900 + 0.3383i & 0.0787 + 0.1229i & -0.1125 + 0.0039i & 0.5154 + 0.0000i \end{pmatrix}, \quad (7)$$

$$\mathcal{C}_2 = \begin{pmatrix} 0.7187 + 0.0000i & -0.1056 + 0.1020i & 0.1736 - 0.0679i & -0.0741 - 0.2666i \\ -0.1056 - 0.1020i & 0.8006 + 0.0000i & -0.1944 - 0.1911i & -0.1028 + 0.1411i \\ 0.1736 + 0.0679i & -0.1944 + 0.1911i & 0.2813 + 0.0000i & 0.1056 - 0.1020i \\ -0.0741 + 0.2666i & -0.1028 - 0.1411i & 0.1056 + 0.1020i & 0.1994 + 0.0000i \end{pmatrix}, \quad (8)$$

$$\mathcal{C}_3 = \begin{pmatrix} 0.5248 + 0.0000i & -0.2288 + 0.1541i & -0.2444 - 0.1881i & -0.2190 + 0.1014i \\ -0.2288 - 0.1541i & 0.3227 + 0.0000i & 0.0601 + 0.0484i & 0.2818 - 0.1173i \\ -0.2444 + 0.1881i & 0.0601 - 0.0484i & 0.4752 + 0.0000i & 0.2288 - 0.1541i \\ -0.2190 - 0.1014i & 0.2818 + 0.1173i & 0.2288 + 0.1541i & 0.6773 + 0.0000i \end{pmatrix}, \quad (9)$$

$$\mathcal{C}_4 = \begin{pmatrix} 0.3788 + 0.0000i & 0.1571 - 0.1211i & -0.3581 - 0.0580i & 0.0979 + 0.0813i \\ 0.1571 + 0.1211i & 0.5037 + 0.0000i & -0.2062 - 0.4069i & 0.3727 + 0.1591i \\ -0.3581 + 0.0580i & -0.2062 + 0.4069i & 0.6212 + 0.0000i & -0.1571 + 0.1211i \\ 0.0979 - 0.0813i & 0.3727 - 0.1591i & -0.1571 - 0.1211i & 0.4963 + 0.0000i \end{pmatrix}, \quad (10)$$

$$\mathcal{C}_5 = \begin{pmatrix} 0.4503 + 0.0000i & 0.1535 - 0.0604i & 0.2019 + 0.1541i & 0.0964 + 0.1834i \\ 0.1535 + 0.0604i & 0.4329 + 0.0000i & -0.0169 + 0.0529i & -0.1842 - 0.0254i \\ 0.2019 - 0.1541i & -0.0169 - 0.0529i & 0.5497 + 0.0000i & -0.1535 + 0.0604i \\ 0.0964 - 0.1834i & -0.1842 + 0.0254i & -0.1535 - 0.0604i & 0.5671 + 0.0000i \end{pmatrix}. \quad (11)$$

Our task is to optimize the parameters specifying the channel decomposition. Parametrization of unitary operator $U \in SU(2)$ is

$$U = e^{-i\theta\vec{n}\cdot\vec{\sigma}} = \cos \theta \mathbf{I} - i \sin \theta (\vec{n} \cdot \vec{\sigma}), \quad (12)$$

For a generalized extreme channel \mathcal{E}_1^c , the initial rotation $R_{\mathbf{m}}^{\mathcal{E}_1^c}(2\delta)$ is parameterized by $\delta^{\mathcal{E}_1^c}$, $m_1^{\mathcal{E}_1^c}$, $m_2^{\mathcal{E}_1^c}$, the final rotation $R_{\mathbf{n}}^{\mathcal{E}_1^c}(2\varphi)$ by $\varphi^{\mathcal{E}_1^c}$, $n_1^{\mathcal{E}_1^c}$, $n_2^{\mathcal{E}_1^c}$, and Kraus operators by $\alpha^{\mathcal{E}_1^c}$ and $\beta^{\mathcal{E}_1^c}$. For generalized extreme channel \mathcal{E}_2^c , the initial rotation

$R_m^{\mathcal{E}_2}(2\delta)$ is parameterized by $\delta^{\mathcal{E}_2}$, $m_1^{\mathcal{E}_2}$, $m_2^{\mathcal{E}_2}$, the final rotation $R_n^{\mathcal{E}_2}(2\varphi)$ by $\varphi^{\mathcal{E}_2}$, $n_1^{\mathcal{E}_2}$, $n_2^{\mathcal{E}_2}$ and Kraus operators by $\alpha^{\mathcal{E}_2}$ and $\beta^{\mathcal{E}_2}$. Simulation results are shown in Table I.

III. EXPERIMENTAL SETUP

Realization of Kraus operators M_i (3) is described by the circuit shown in Fig. 1a and implemented according to the schematic of Fig. 1b. A femtosecond pulse (150fs, 80MHz, 780nm) is converted to ultraviolet pulses (390nm) through a frequency doubler LiB_3O_5 crystal. Then the ultraviolet pulse (150fs, 80MHz, 390 nm) passes through two 2-mm-thick collinear BBO crystals, creating two pairs of photons $|HV\rangle_{ij}$ with central wavelength of 780nm. The ultraviolet pulse (390nm) and the generated photons (780nm) are along the same direction and separated by a dichroic mirror (DM).

The generated photons $|HV\rangle_{ij}$ are separated by a PBS and the reflected photons are detected to guarantee that the transmitted photons are underway. All four photons are collected by the SMF and detected by the SPCM. All the photons are filtered by narrowband interference filters with $\Delta\lambda_{\text{FWHM}} = 2.8\text{nm}$ (fullwidth at half-maximum) prior to detection. Throughout the entire experiment, the two-fold coincidence rates for $|HV\rangle_{12}$ and $|HV\rangle_{34}$ are $9 \times 10^4\text{s}^{-1}$ and $10 \times 10^4\text{s}^{-1}$, respectively. Overall detective efficiency is approximately 19%. We use a homemade Field Programmable Gate Array (FPGA) to record the fourfold coincidence (not shown here).

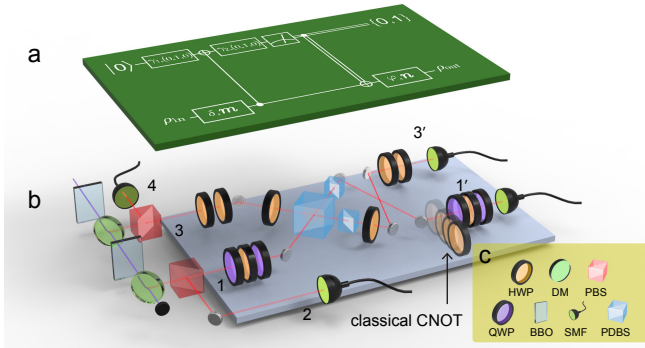


FIG. 1: **Experimental scheme for quantum channel simulation.** **a**, The quantum circuit for M_i (3), comprising single-qubit rotations, one quantum CNOT gate, and one classical CNOT gate. When the measurement result on ancilla is $|0\rangle$ ($|1\rangle$), the circuit postselectively acts as M_0 (M_1). **(b)** Schematic drawing of the experimental setup. **(c)** Symbols used in **b**.

The single-photon rotation gates are realized by the combination of half-wave plates (HWPs) and quarter-wave plates (QWPs). The effect of HWP and QWP whose fast axes are at angles τ and ξ with respect to the vertical axis, respectively,

are given by the 2×2 matrices,

$$U_{\text{HWP}}(\tau) = \begin{pmatrix} \cos 2\tau & -\sin 2\tau \\ -\sin 2\tau & \cos 2\tau \end{pmatrix}, \quad (13)$$

$$U_{\text{QWP}}(\xi) = \begin{pmatrix} 1 + i \cos 2\xi & -i \sin 2\xi \\ -i \sin 2\xi & 1 - i \cos 2\xi \end{pmatrix} / \sqrt{2}$$

The rotation around the y axis by angle $2\gamma_i$ is

$$R_y(2\gamma_i) = e^{-i\gamma_i Y} = \cos \gamma_i \mathbb{1} - i \sin \gamma_i Y. \quad (14)$$

The combinational operation of two HWPs set at 0° and τ , respectively, is in the form

$$U_{\text{HWP}}(0^\circ) \cdot U_{\text{HWP}}(\tau) = \begin{pmatrix} \cos 2\tau & -\sin 2\tau \\ \sin 2\tau & \cos 2\tau \end{pmatrix}. \quad (15)$$

We set $\tau = \gamma_i/2$; then the operation is $R_y(2\gamma_i)$.

The rotation around

$$\mathbf{r} \cdot \boldsymbol{\sigma} = AX + BY + CZ \quad (16)$$

by angle 2θ , where A , B and C satisfy $A^2 + B^2 + C^2 = 1$, can be implemented by a HWP set at angle τ sandwiched by two QWPs set at angles ξ_1 and ξ_2 , respectively. The combinational operation of the three wave plates is

$$U_{\text{QWP}}(\xi_1)U_{\text{HWP}}(\tau)U_{\text{QWP}}(\xi_2) = \begin{pmatrix} \cos \theta - iC \sin \theta & -\sin \theta(iA + B) \\ -\sin \theta(iA - B) & \cos \theta - iC \sin \theta \end{pmatrix} \quad (17)$$

where

$$\cos \theta = \cos \Theta \cos \Lambda, \quad A = \sin \Theta \cos \Lambda / \sqrt{\Omega},$$

$$B = \cos \Theta \sin \Lambda / \sqrt{\Omega}, \quad C = \sin \Theta \sin \Lambda / \sqrt{\Omega} \quad (18)$$

with

$$\Theta = \xi_1 - \xi_2, \quad \Lambda = 2\tau - \xi_1 - \xi_2, \quad \Omega = 1 - \cos^2 \Theta \cos^2 \Lambda. \quad (19)$$

By appropriately choosing the angles τ , ξ_1 and ξ_2 , rotation $R_r(2\theta)$ can be implemented.

The two-photon controlled NOT (CNOT) gate [25] are realized by overlapping two photons on a polarization-dependent beamsplitter (PDBS). The system and ancilla photonic qubits are generated by shining the ultraviolet pluses on two collinear β -barium borate (BBO) crystals emitting photon pairs $|HV\rangle_{ij}$ along the pumping direction, with $|H\rangle$ and $|V\rangle$ the horizontal and vertical-polarization states, and i, j denote the path mode. The generated photons in the pair $|HV\rangle_{ij}$ are separated by a polarizing beam splitter (PBS), which transmits the $|H\rangle$ component and reflects the $|V\rangle$ component for each photon. Reflected photons 2 and 4 are collected by single-mode fibers (SMFs) and detected by single-photon counting modules (SPCMs) to herald that photons 1 (system) and 3 (ancilla) are underway, respectively [26].

	\mathcal{C}_1	\mathcal{C}_2	\mathcal{C}_3	\mathcal{C}_4	\mathcal{C}_5		\mathcal{C}_1	\mathcal{C}_2	\mathcal{C}_3	\mathcal{C}_4	\mathcal{C}_5
$m_1^{\mathcal{E}_1}$	0.1043	0.5254	0.9756	0.7444	0.2633	$\beta^{\mathcal{E}_1}$	3.3938	3.7248	3.9264	2.5101	3.6886
$m_2^{\mathcal{E}_1}$	0.2658	0.7401	0.2193	0.1878	0.2494	$\alpha^{\mathcal{E}_2}$	5.3916	2.5514	0.7277	1.5968	1.6137
$n_1^{\mathcal{E}_1}$	0.3944	0.1263	0.5393	0.9714	0.1862	$\beta^{\mathcal{E}_2}$	3.1851	6.2832	3.2350	4.0102	4.0769
$n_2^{\mathcal{E}_1}$	0.9124	0.9920	0.4951	0.2373	0.5166	$\delta^{\mathcal{E}_1}$	5.6926	4.7360	2.3722	1.7879	2.5147
$m_1^{\mathcal{E}_2}$	0.9768	0.0000	0.7061	0.8913	0.0120	$\varphi^{\mathcal{E}_1}$	6.1559	3.1887	2.2483	0.3786	4.5601
$m_2^{\mathcal{E}_2}$	0.2148	0.9502	0.6602	0.0000	0.4274	$\delta^{\mathcal{E}_2}$	0.1796	3.9477	0.5693	1.4948	1.1443
$n_1^{\mathcal{E}_2}$	0.8214	0.2991	0.2434	0.7347	0.4465	$\varphi^{\mathcal{E}_2}$	3.4528	1.7924	4.7052	4.5230	1.7113
$n_2^{\mathcal{E}_2}$	0.5598	0.4585	0.7350	0.4100	0.8948	p	0.4675	0.7001	0.8370	0.9032	0.4922
$\alpha^{\mathcal{E}_1}$	3.8118	4.7982	6.1211	5.8303	5.4589	ϵ	0.0031	0.0009	0.0040	0.0006	0.0045

TABLE I: Numerical simulation of the channel decomposition for five randomly chosen input channels and channel \mathcal{C}_T . Error ϵ is the actual error from the simulation.

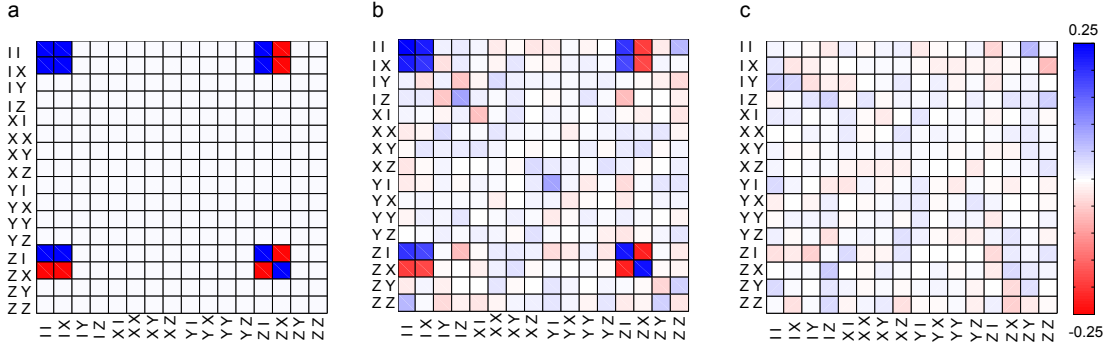


FIG. 2: **Process matrix of the CNOT operation.** **a.** Real elements of ideal process matrix (imaginary elements are identically zero). **b.** The real elements of χ_{exp} . **c.** Imaginary elements of χ_{exp} .

We experimentally characterize the quantum CNOT gate via quantum process tomography (QPT) technology [27] and obtain gate fidelity $F = 0.83 \pm 0.02$ as shown in Fig.2

The classical CNOT operation is a classical logic operation that flips the system-qubit state $1'$ conditioned on the measurement result of ancillary qubit $3'$. Experimentally, classical CNOT is effectively statistically simulated: we set the measurement basis of ancillary photon $3'$ on $|H\rangle$ or $|V\rangle$ with equal probability. No further operation on system qubit $1'$ occurs when the measurement basis choice of ancillary photon $3'$ is $|H\rangle$, whereas an X operation (an HWP set at 45°) is applied on the system qubit $1'$ when the measurement basis choice of ancillary photon $3'$ is $|V\rangle$. If the ancilla-qubit measurement result is $|H\rangle$ ($|V\rangle$), the simulator is described by M_0 (M_1).

The probability p is also statistically simulated. We first set up the circuit for simulating \mathcal{E}_1^c and collect data for time t_1 . Then we convert the circuit to the case of simulating \mathcal{E}_2^c and collect data for time t_2 . Combining these data yields $\mathcal{E}(\rho) = (t_1\mathcal{E}_1^c + t_2\mathcal{E}_2^c)/(t_1 + t_2)$. By choosing t_1 and t_2 appropriately, any $p \in [0, 1]$ can thus be simulated.

We emphasise here that the rotations in our experiment are realized manually, and the classical CNOT gate is implemented by inserting an HWP according to the projector choice on photon $3'$. The mixture of \mathcal{E}_1^c and \mathcal{E}_2^c is statistically simu-

lated by collecting data from \mathcal{E}_1^c and \mathcal{E}_2^c with different times. In our experiment, simulating one single-qubit channel needs us to run the setup four times and then combine the collected data.

In fact, the four runs can be embedded into one run. Here, we also propose an experimental scheme to simulate any single-qubit channel within one run. Below we summarize the experimental scheme. As shown in Fig. 3, a beam of light with two different colors, with central wavelength of λ_1 and λ_2 respectively, is split by a dichroic mirror(DM). The transmitted color λ_1 go through \mathcal{E}_1^c as shown in Fig. 1. The reflected color λ_2 first go to an automatically controlled attenuator and then go through \mathcal{E}_1^c . The attenuator setting depends on the parameter $p \in [0, 1]$. For example, the attenuator block half of λ_2 is equivalence of simulating $p = 2/3$. Finally, λ_1 and λ_2 is re-combined on another DM and injected to the detector. All the rotations can be realized by an automatically controlled waveplate and the classical CNOT can be replaced by feedforward technology.

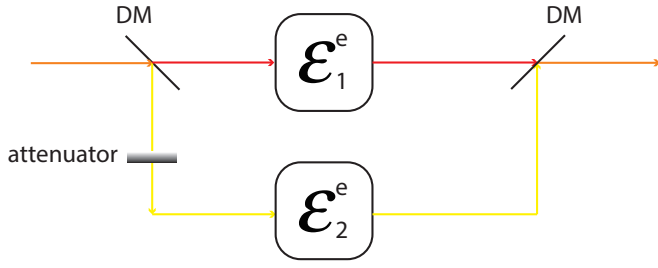


FIG. 3: Proposed experimental scheme to simulate single-qubit channel with one run.

$$\mathcal{E} = \begin{pmatrix} 0.3938 & 0.0075 + 0.0739i & 0.0172 + 0.0155i & 0.0801 - 0.0614i \\ 0.0075 - 0.0739i & 0.1594 & -0.0733 - 0.0801i & -0.066 + 0.0172i \\ 0.0172 - 0.0155i & -0.0733 + 0.0801i & 0.2241 & -0.014 - 0.075i \\ 0.0801 + 0.0614i & -0.066 - 0.0172i & -0.014 + 0.075i & 0.2228 \end{pmatrix} \quad (20)$$

$m_1^{\mathcal{E}_1}$	0.1896
$m_2^{\mathcal{E}_1}$	0.7948
$n_1^{\mathcal{E}_1}$	-0.7813
$n_2^{\mathcal{E}_1}$	0.5804
$m_1^{\mathcal{E}_2}$	0.3901
$m_2^{\mathcal{E}_2}$	0.5051
$n_1^{\mathcal{E}_2}$	-0.0919
$n_2^{\mathcal{E}_2}$	0.9817
$\alpha^{\mathcal{E}_1}$	0.18π
$\beta^{\mathcal{E}_1}$	0.26π
$\alpha^{\mathcal{E}_2}$	0.84π
$\beta^{\mathcal{E}_2}$	0.40π
$\delta^{\mathcal{E}_1}$	0.42π
$\varphi^{\mathcal{E}_1}$	0.36π
$\delta^{\mathcal{E}_2}$	-0.75π
$\varphi^{\mathcal{E}_2}$	0.56π
p	0.6

TABLE II: Decomposition of channel \mathcal{E}

is realized by the circuit in Fig. 1b with appropriate parameters specified. The decomposition of \mathcal{E} is shown in Table II. For $p = 0.6$, we set $t_1 = 60$ s and $t_2 = 40$ s.

To verify accurate channel simulation, we use QPT to reconstruct the matrix representation of \mathcal{E} . Figure 4 shows the experimentally reconstructed \mathcal{E}_{exp} matrix. We calculate the process fidelity

$$F_p = \text{Tr} \left(\sqrt{\sqrt{\mathcal{E}} \mathcal{E}_{\text{exp}} \sqrt{\mathcal{E}}} \right)^2 \quad (21)$$

between the reconstructed matrix \mathcal{E}_{exp} and \mathcal{E} and discover $F_p = 0.94 \pm 0.02$.

IV. RESULTS

A. Random channel

We first show that a randomly chosen channel is accurately simulated with our setup. Randomly chosen input channel \mathcal{E}

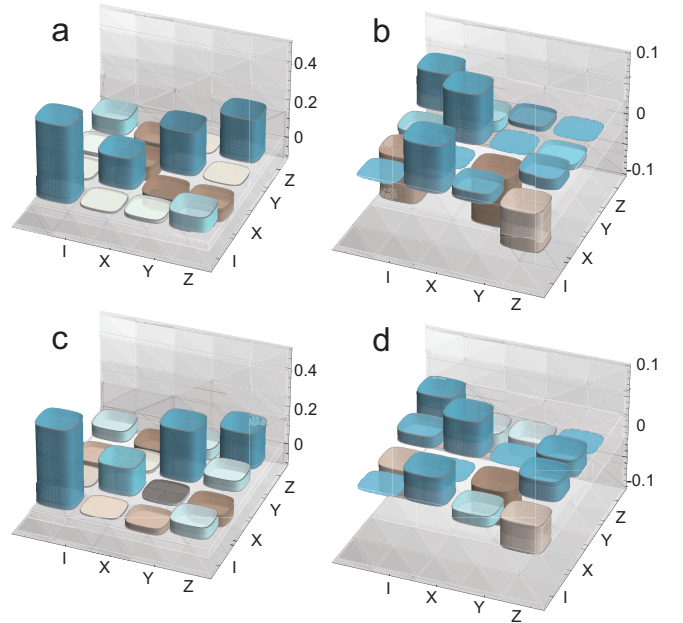


FIG. 4: Reconstructed process matrix of the randomly chosen channel in Eq. (20). (a) The real part of the ideal channel \mathcal{E} . (b) The imaginary part of the ideal channel \mathcal{E} . (c) The real part of the experimentally constructed channel \mathcal{E}_{exp} . (d) The imaginary part of the experimentally constructed channel \mathcal{E}_{exp} .

Average fidelity is [28]

$$\bar{F} = (2F_p + 1)/3 = 0.96 \pm 0.01. \quad (22)$$

As further analysis, we calculate the trace distance

$$D(\mathcal{E}, \mathcal{E}_{\text{exp}}) = \text{Tr} |\mathcal{E} - \mathcal{E}_{\text{exp}}|/2 = 0.22 \pm 0.02. \quad (23)$$

Fidelity F_p is related to D by the inequality [13]

$$1 - \sqrt{F_p} \leq D \leq \sqrt{1 - F_p}. \quad (24)$$

In our case ($F_p = 0.94$), the upper and lower bounds of D are 0.06 and 0.24.

B. Amplitude Damping Channel

The amplitude damping (AD), or decay channel can be determined by two Kraus operators

$$K_0 = \begin{pmatrix} 1 & 0 \\ 0 & \sqrt{1-\lambda} \end{pmatrix}, K_1 = \begin{pmatrix} 0 & \sqrt{\lambda} \\ 0 & 0 \end{pmatrix}. \quad (25)$$

Table III shows the setting of parameters of the simulator. Fig. 5a(e) shows the geometric interpre-

λ	\mathcal{E}_1^e						p
	α	β	γ_1	γ_2	$R_m(2\delta)$	$R_n(2\varphi)$	
0	0	0	$\pi/4$	$-\pi/4$	none	none	1
0.36	0.103π	0	0.2π	-0.2π	none	none	1
0.5	$\pi/4$	0	$3\pi/8$	$-3\pi/8$	none	none	1
0.75	$\pi/3$	0	$\pi/12$	$-\pi/12$	none	none	1
1	$\pi/2$	0	0	0	none	none	1

TABLE III: Parameters of amplitude damping channel for the given λ .

tation of ideal(experimental) AD channel for $\lambda \in \{0, 0.36, 0.5, 0.75, 1\}$.

C. Bit-flip channel

The bit-flip channel has two Kraus operators in the form

$$K_0 = \sqrt{1-\lambda}\mathbb{1} = \begin{pmatrix} \sqrt{1-\lambda} & 0 \\ 0 & \sqrt{1-\lambda} \end{pmatrix}, \quad (26)$$

$$K_1 = \sqrt{\lambda}X = \begin{pmatrix} 0 & \sqrt{\lambda} \\ \sqrt{\lambda} & 0 \end{pmatrix}.$$

For different λ , the corresponding channel parameters are shown in Table IV. Fig. 5b(f) shows the geometric interpretation of ideal(experimental) bit-flip channel for $\lambda \in \{0, 0.36, 0.5, 0.75, 1\}$.

D. Phase-flip channel

The phase-flip channel has two Kraus operators in the form,

$$K_0 = \sqrt{1-\lambda}\mathbb{1} = \begin{pmatrix} \sqrt{1-\lambda} & 0 \\ 0 & \sqrt{1-\lambda} \end{pmatrix}, \quad (27)$$

$$K_1 = \sqrt{\lambda}Z = \begin{pmatrix} \sqrt{\lambda} & 0 \\ 0 & -\sqrt{\lambda} \end{pmatrix}.$$

λ	\mathcal{E}_1^e						p
	α	β	γ_1	γ_2	$R_m(2\delta)$	$R_n(2\varphi)$	
0	0	0	$\pi/4$	$-\pi/4$	none	none	1
0.36	0.103π	0.103π	$\pi/4$	-0.044π	none	none	1
0.5	$\pi/4$	$\pi/4$	$\pi/4$	0	none	none	1
0.75	$\pi/3$	$\pi/3$	$\pi/4$	$\pi/12$	none	none	1
1	$\pi/2$	$\pi/2$	$\pi/4$	$\pi/4$	none	none	1

TABLE IV: Parameters of bit-flip channel for the given λ .

For different λ , the setting of the parameters are shown in Table V. Fig. 5c(g) shows the geometric interpretation of ideal(experimental) phase-flip channel for $\lambda \in \{0, 0.36, 0.5, 0.75, 1\}$.

E. Depolarizing channel

The depolarizing channel, which is known as a white-noise channel, has the form

$$\mathcal{E}(\rho) = (1-\lambda)\rho + \frac{\lambda}{3}(X\rho X + Y\rho Y + Z\rho Z). \quad (28)$$

The setting of the parameters are shown in Table VI. Fig. 5e(h) shows the geometric interpretation of ideal(experimental) depolarizing channel for $\lambda \in \{0, 0.36, 0.5, 0.75, 1\}$.

F. Weak measurement

We show that our apparatus successfully simulates trace-decreasing channels, such as weak measurement followed by measurement reversal, which is a strategy for offsetting amplitude damping \mathcal{E}_{AD} (25) at the cost of losing particles through postselection [18, 19, 29]. For a single-qubit input state ρ , this strategy is

$$\rho \mapsto \rho' = N[\mathcal{E}_{AD}(M\rho M^\dagger)]N^\dagger \quad (29)$$

for weak measurement $M = \text{diag}(1, \sqrt{1-p_1})$ with $p_1 \sim 0$ and weak measurement reversal $N = \text{diag}(\sqrt{1-p_2}, 1)$ with $p_2 \sim 0$. A successful outcome corresponds to high fidelity $\text{Tr}(\sqrt{\sqrt{\rho'}\rho\sqrt{\rho'}})^2$ with success probability $\text{Tr}\rho'$.

Larger p_1 corresponds to superior protection and smaller success probability. Seeking to explore the trade-off between success probability and weak measurement strength p_1 , we choose a fairly strong measurement strength $p_1 = 0.8$ and then let $p_2 = p_1 + \lambda(1-p_1)$ if damping parameter λ is given (this relation between p_1 and p_2 is the ‘‘optimal strategy’’); otherwise $p_2 = p_1$ if λ is unknown (the ‘‘non-optimal strategy’’ [30]. Theoretical and experimental state fidelity results for input states $|H\rangle, |V\rangle, |D\rangle = 1/\sqrt{2}(|H\rangle + |V\rangle)$ and $|L\rangle = 1/\sqrt{2}(|H\rangle + i|V\rangle)$ are shown in Fig. 6 for three cases: pure amplitude damping, non-optimal measurement strategy, and optimal measurement strategy. Note that $|H\rangle$

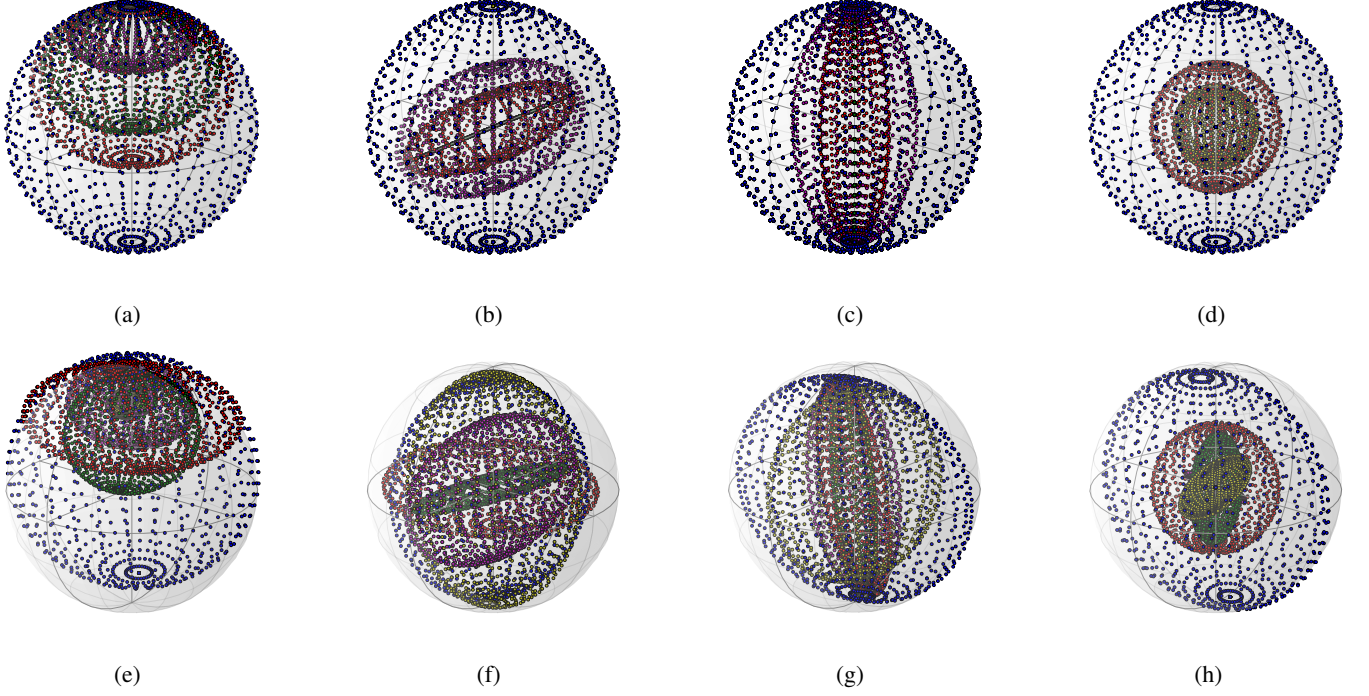


FIG. 5: The geometric interpretation of the quantum-noise channels on a Bloch sphere. (a)–(d), the ideal geometric interpretations of amplitude damping channel, bit-flip channel, phase-flip channel and depolarizing channel with $\lambda = 0$ (blue dots), $\lambda = 0.36$ (red dots), $\lambda = 0.5$ (green dots), $\lambda = 0.75$ (purple dots) and $\lambda = 1$ (yellow dots). (e)–(f), the geometric interpretations of experimentally reconstructed channels.

λ	\mathcal{E}_1^c						\mathcal{E}_2^c						p
	α	β	γ_1	γ_2	$R_m(\delta)$	$R_n(\psi)$	α	β	γ_1	γ_2	$R_m(\delta)$	$R_n(\psi)$	
0	0	0	$\pi/4$	$-\pi/4$	none	none	π	0	$-\pi/4$	$\pi/4$	none	none	1
0.36	0	0	$\pi/4$	$-\pi/4$	none	none	π	0	$-\pi/4$	$\pi/4$	none	none	0.64
0.5	0	0	$\pi/4$	$-\pi/4$	none	none	π	0	$-\pi/4$	$\pi/4$	none	none	0.5
0.75	0	0	$\pi/4$	$-\pi/4$	none	none	π	0	$-\pi/4$	$\pi/4$	none	none	0.25
1	0	0	$\pi/4$	$-\pi/4$	none	none	π	0	$-\pi/4$	$\pi/4$	none	none	1

TABLE V: Parameters of phase-flip channel for the given λ .

input is immune to \mathcal{E}_{AD} , but, due to experimental imperfection, the fidelity for input state $|H\rangle$ is not exactly 1. We find that the optimal strategy provides the best protection, and the experimental results agree with the theory for all three cases.

V. CONCLUSION

In this article, we demonstrate that a digital channel simulator can be realized via linear optics. Any open-system quantum dynamics and quantum channels on single qubit can be simulated in our system. For multi-qubit channel simulation, decomposition algorithm has been extended to qudit channels[31]. In large-scale channel simulation, linear optics system might be retarded by the probabilistic CNOT gate. However, other systems, such as superconducting qubit and trapped ions, can benefit from our results. Our demonstration can serve as a foundation for future experimental simulations

employing networks of qubit channel simulators. Such networks could serve to simulate general dissipative many-body dynamics including the interplay between dissipative and unitary processes [32] and dissipative universal quantum computation [12] by combining two-qubit entangling gates with the qubit-channel simulators.

Acknowledgments

We acknowledge insightful discussions with I. Dhand, W.-J. Zou, Y. Chen and H.-H. Wang. This work has been supported by the National Natural Science Foundation of China, the Chinese Academy of Sciences, and the National Fundamental Research Program (grant no. 11404318 and no. 2011CB921300). H. L. was partially supported by Shanghai Sailing Program. X.-C. Y. was also supported by the Alexander von Humboldt Foundation. and B.C.S. acknowledges fi-

λ	\mathcal{E}_1^c						\mathcal{E}_2^c						p
	α	β	γ_1	γ_2	$R_m(\delta)$	$R_n(\psi)$	α	β	γ_1	γ_2	$R_m(\delta)$	$R_n(\psi)$	
0	0	0	$\pi/4$	$-\pi/4$	none	none	$\pi/4$	$\pi/4$	$\pi/4$	0	Y	none	1
0.36	0.13π	0.13π	$\pi/4$	$-0.12\pi/$	none	none	$\pi/4$	$\pi/4$	$\pi/4$	0	Y	none	0.76
0.5	$\pi/6$	$\pi/6$	$\pi/4$	$-\pi/12$	none	none	$\pi/4$	$\pi/4$	$\pi/4$	0	Y	none	0.66
0.75	$\pi/4$	$\pi/4$	$\pi/4$	0	none	none	$\pi/4$	$\pi/4$	$\pi/4$	0	Y	none	0.5
1	$\pi/2$	$\pi/2$	$\pi/4$	$\pi/4$	none	none	$\pi/4$	$\pi/4$	$\pi/4$	0	Y	none	0.33

TABLE VI: Parameters of depolarizing channel for the given λ .

nancial support from the 1000 Talent Plan, NSERC and AITF.

-
- [1] R. P. Feynman, *Int. J. Theor. Phys.* **21**(6/7), 467 (1982).
- [2] S. Lloyd, *Science* **273**(5278), 1073 (1996).
- [3] I. Buluta and F. Nori, *Science* **326**(5949), 108 (2009).
- [4] A. Aspuru-Guzik and P. Walther, *Nat Phys* **8**(4), 285 (2012), URL <http://dx.doi.org/10.1038/nphys2253>.
- [5] J. I. Cirac and P. Zoller, *Nat. Phys.* **8**(2275), 264 (2012).
- [6] R. Blatt and C. F. Roos, *Nat. Phys.* **8**(4), 277 (2012), URL <http://dx.doi.org/10.1038/nphys2252>.
- [7] T. Prosen and E. Ilievski, *Phys. Rev. Lett.* **107**, 060403 (2011), URL <http://link.aps.org/doi/10.1103/PhysRevLett.107.060403>.
- [8] S. Diehl, A. Micheli, A. Kantian, B. Kraus, H. P. Buchler, and P. Zoller, *Nat. Phys.* **4**(11), 878 (2008), URL <http://dx.doi.org/10.1038/nphys1073>.
- [9] B. M. Terhal and D. P. DiVincenzo, *Phys. Rev. A* **61**(2), 022301 (2000), URL <http://link.aps.org/doi/10.1103/PhysRevA.61.022301>.
- [10] H. Lu, L.-K. Chen, C. Liu, P. Xu, X.-C. Yao, L. Li, N.-L. Liu, B. Zhao, Y.-A. Chen, and J.-W. Pan, *Nat. Photon.* **8**(5), 364 (2014), URL <http://dx.doi.org/10.1038/nphoton.2014.81>.
- [11] B.-H. Liu, L. Li, Y.-F. Huang, C.-F. Li, G.-C. Guo, E.-M. Laine, H.-P. Breuer, and J. Piilo, *Nat. Phys.* **7**(12), 931 (2011), URL <http://dx.doi.org/10.1038/nphys2085>.
- [12] F. Verstraete, M. M. Wolf, and J. I. Cirac, *Nat. Phys.* **5**(9), 633 (2009).
- [13] M. A. Nielsen and I. L. Chuang, *Quantum Computation and Quantum Information* (Cambridge University Press, Cambridge U.K., 2000).
- [14] J. Carolan, C. Harrold, C. Sparrow, E. Martín-López, N. J. Russell, J. W. Silverstone, P. J. Shadbolt, N. Matsuda, M. Oguma, M. Itoh, G. D. Marshall, M. G. Thompson, *et al.*, *Science* **349**(6249), 711 (2015), ISSN 0036-8075, URL <http://science.sciencemag.org/content/349/6249/711>, <http://science.sciencemag.org/content/349/6249/711.full.pdf>.
- [15] Y.-C. Jeong, J.-C. Lee, and Y.-H. Kim, *Phys. Rev. A* **87**, 014301 (2013), URL <http://link.aps.org/doi/10.1103/PhysRevA.87.014301>.
- [16] A. Shaham and H. S. Eisenberg, *Opt. Lett.* **37**(13), 2643 (2012), URL <http://ol.osa.org/abstract.cfm?URI=ol-37-13-2643>.
- [17] A. Shaham and H. S. Eisenberg, *Phys. Rev. A* **83**, 022303 (2011), URL <http://link.aps.org/doi/10.1103/PhysRevA.83.022303>.
- [18] Y.-S. Kim, J.-C. Lee, O. Kwon, and Y.-H. Kim, *Nat. Phys.* **8**(2), 117 (2012), URL <http://dx.doi.org/10.1038/nphys2178>.
- [19] Y.-S. Kim, Y.-W. Cho, Y.-S. Ra, and Y.-H. Kim, *Opt. Express* **17**(14), 11978 (2009), URL <http://www.opticsexpress.org/abstract.cfm?URI=oe-17-14-11978>.
- [20] F. Sciarrino, C. Sias, M. Ricci, and F. De Martini, *Phys. Rev. A* **70**, 052305 (2004), URL <http://link.aps.org/doi/10.1103/PhysRevA.70.052305>.
- [21] H.-T. Lim, Y.-S. Ra, Y.-S. Kim, J. Bae, and Y.-H. Kim, *Phys. Rev. A* **83**, 020301 (2011), URL <http://link.aps.org/doi/10.1103/PhysRevA.83.020301>.
- [22] H.-T. Lim, Y.-S. Kim, Y.-S. Ra, J. Bae, and Y.-H. Kim, *Phys. Rev. Lett.* **107**, 160401 (2011), URL <http://link.aps.org/doi/10.1103/PhysRevLett.107.160401>.
- [23] M. Möttönen and J. J. Vartiainen, *Trends in Quantum Computing Research* (Nova, New York, 2006), chap.7.
- [24] D.-S. Wang, D. W. Berry, M. C. de Oliveira, and B. C. Sanders, *Phys. Rev. Lett.* **111**, 130504 (2013).
- [25] J. L. O'Brien, G. J. Pryde, A. G. White, T. C. Ralph, and D. Branning, *Nature* **426**(6964), 264 (2003).
- [26] P. G. Kwiat, K. Mattle, H. Weinfurter, A. Zeilinger, A. V. Sergienko, and Y. Shih, *Phys. Rev. Lett.* **75**, 4337 (1995), URL <http://link.aps.org/doi/10.1103/PhysRevLett.75.4337>.
- [27] J. L. O'Brien, G. J. Pryde, A. Gilchrist, D. F. V. James, N. K. Langford, T. C. Ralph, and A. G. White, *Phys. Rev. Lett.* **93**, 080502 (2004), URL <http://link.aps.org/doi/10.1103/PhysRevLett.93.080502>.
- [28] M. D. Bowdrey, D. K. Oi, A. J. Short, K. Banaszek, and J. A. Jones, *Physics Letters A* **294**(5), 258 (2002).
- [29] A. N. Korotkov and K. Keane, *Phys. Rev. A* **81**, 040103 (2010), URL <http://link.aps.org/doi/10.1103/PhysRevA.81.040103>.
- [30] S.-C. Wang, Z.-W. Yu, W.-J. Zou, and X.-B. Wang, *Phys. Rev. A* **89**, 022318 (2014), URL <http://link.aps.org/doi/10.1103/PhysRevA.89.022318>.
- [31] D.-S. Wang and B. C. Sanders, *New J. Phys.* **17**(4), 043004 (2015).
- [32] E. G. Dalla Torre, E. Demler, T. Giamarchi, and E. Altman, *Nat. Phys.* **6**(10), 806 (2010).

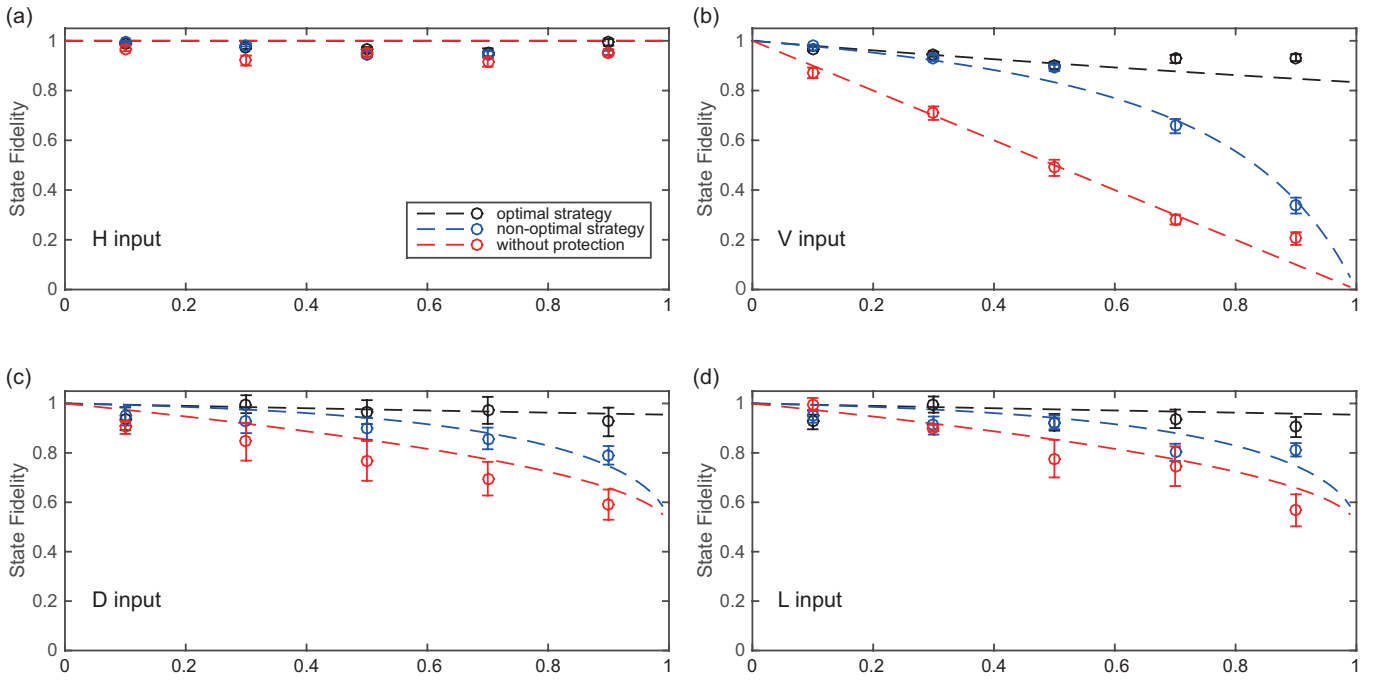


FIG. 6: State-fidelity dynamics for the amplitude-damping channel with weak measurement protection. Dashed lines represent theoretical results, and dots represent experimental results. Red, blue and black colors represent no weak measurement, non-optimal measurement strategy ($p_1 = p_2$) and optimal measurement strategy ($p_2 = p_1 + \lambda(1 - p_1)$), respectively. The input state is (a) $|H\rangle$, (b) $|V\rangle$, (c) $|D\rangle$, and (d) $|L\rangle$